The Astronomical Journal, 152:200 (15pp), 2016 December doi:10.3847/0004-6256/152/6/200

A SEARCH FOR MASS LOSS ON THE CEPHEID INSTABILITY STRIP USING H I 21 cm LINE OBSERVATIONS

L. D. Matthews[1], M. Marengo[2], and N. R. Evans[3]

[1] MIT Haystack Observatory, Off Route 40, Westford, MA 01886, USA; lmatthew@haystack.mit.edu

[2] Department of Physics & Astronomy, Iowa State University, Ames, IA 50011, USA

[3] Harvard-Smithsonian Center for Astrophysics, 60 Garden Street, MS-42, Cambridge, MA 02138, USA

Received 2016 August 15; revised 2016 September 19; accepted 2016 September 19; published 2016 December 2

ABSTRACT

We present the results of a search for H I 21 cm line emission from the circumstellar environments of four Galactic Cepheids (RS Pup, X Cyg, ζ Gem, and T Mon) based on observations with the Karl G. Jansky Very Large Array. The observations were aimed at detecting gas associated with previous or ongoing mass loss. Near the long-period Cepheid T Mon, we report the detection of a partial shell-like structure whose properties appear consistent with originating from an earlier epoch of Cepheid mass loss. At the distance of T Mon, the nebula would have a mass (H I+He) of $\sim 0.5 M_{\odot}$, or ~6% of the stellar mass. Assuming that one-third of the nebular mass comprises swept-up interstellar gas, we estimate an implied mass-loss rate of $\dot{M} \sim (0.6\text{–}2) \times 10^{-5}\ M_{\odot}\ \mathrm{yr}^{-1}$. No clear signatures of circumstellar emission were found toward ζ Gem, RS Pup, or X Cyg, although in each case, line-of-sight confusion compromised portions of the spectral band. For the undetected stars, we derive model-dependent 3σ upper limits on the mass-loss rates, averaged over their lifetimes on the instability strip, of $\lesssim (0.3\text{–}6) \times 10^{-6}\ M_{\odot}\ \mathrm{yr}^{-1}$ and estimate the total amount of mass lost to be less than a few percent of the stellar mass.

Key words: circumstellar matter – radio lines: stars – stars: mass-loss – stars: variables: Cepheids

1. INTRODUCTION

Cepheid variables serve as fundamental calibrators of the cosmic distance scale, making these stars of vital importance to extragalactic astronomy and cosmology (Freedman et al. 2001; Di Benedetto 2013 and references therein). However, important gaps remain in our understanding of the physics and evolution of Cepheids.

One of the most confounding puzzles is the decades-old problem known as the "Cepheid mass discrepancy": mass estimates based on stellar evolution models are inconsistent with pulsation masses (derived from the mass-dependent Period–Luminosity relation) and with masses inferred from orbital dynamics (e.g., Christy 1968; Cox 1980; Pietrzyński et al. 2010). Discrepancies of ~10%–20% have persisted despite continued improvements in evolutionary models (e.g., Bono et al. 2002; Caputo et al. 2005; Keller & Wood 2006; Neilson et al. 2011). Proposed solutions have included extra mixing, rotation, the need for better radiative opacities, and perhaps most importantly, *mass loss* (e.g., Cox 1980; Bono et al. 2006; Neilson et al. 2011, 2012a, 2012b).

If mass loss is occurring during the Cepheid evolutionary phase, this could have important implications for the use of Cepheids as distance indicators, since the presence of circumstellar material may add scatter to inferred luminosities in the form of extra extinction in the visible and excess emission at IR wavelengths (Neilson et al. 2009; Gallenne et al. 2013; Schmidt 2015). Indeed, accounting for these effects may be key to resolving the discrepancy between the Hubble constant determination from Cepheids compared with that derived from Cosmic Microwave Background measurements (e.g., Riess et al. 2016). Mass loss on the instability strip would also impact other evolutionary stages of intermediate mass stars, including the relative lifetimes of the red and blue supergiant phases (e.g., Dohm-Palmer & Skillman 2002), and the determination of what is the maximum initial mass of a star that will end its life as a white dwarf rather than a supernova.

While Cepheid mass loss has been suspected for decades (see review by Cox 1980), the direct and unambiguous detection of escaped or outflowing material from Cepheids has proved to be challenging, leading to empirically estimated mass-loss rates (or upper limits) spanning several orders of magnitude ($\dot{M} \lesssim 10^{-12}$ to $10^{-5} M_{\odot}\ \mathrm{yr}^{-1}$; McAlary & Welch 1986; Deasy 1988; Welch & Duric 1988; Böhm-Vitense & Love 1994; Neilson et al. 2009). However, a series of recent studies has provided mounting evidence that not only is mass loss common for stars on the instability strip, but it typically occurs at rates high enough to significantly impact the star's evolutionary track.

In a study based on *Spitzer* infrared (IR) imaging data, Marengo et al. (2010b) reported the discovery of a bow shock surrounding the Cepheid archetype δ Cephei (δ Cep), providing direct evidence for the existence of a stellar wind, and hence, ongoing mass loss at a rate of $\sim 10^{-7} M_{\odot}\ \mathrm{yr}^{-1}$. Extended IR emission was also detected with *Spitzer* around several other Cepheids by Barmby et al. (2011), including three stars with extended emission seen in multiple IR bands and four other stars with evidence for extended emission in at least one band. In addition, on scales closer to the star, near- and mid-IR interferometry have revealed what appear to be warm, dusty circumstellar envelopes on scales ranging from a few stellar radii (Kervella et al. 2006; Mérand et al. 2006; Gallenne et al. 2013) to several hundred astronomical units (Kervella et al. 2009).

As noted by some authors (e.g., Schmidt 2015), observed IR excesses and extended IR emission are not necessarily a *direct* product of ongoing mass loss, particularly dusty mass loss. For example, in the case of δ Cep, the extended IR nebulosity may be somehow linked with the presence of a binary companion (Anderson et al. 2015), while in the case of RS Pup, the vast circumstellar nebulosity may represent a pre-existing interstellar cloud (Kervella et al. 2009). However, in both of these

Table 1
Properties of the Target Stars

Name	α(J2000.0)	δ(J2000.0)	l	b	$V_{\star,\mathrm{LSR}}$	d	P	M	$R_\star$	V_{3D}	PA	Known
			(°)	(°)	(km s^{-1})	(pc)	(days)	($M_\odot$)	($R_\odot$)	(km s^{-1})	(°)	Binary?
(1)	(2)	(3)	(4)	(5)	(6)	(7)	(8)	(9)	(10)	(11)	(12)	(13)
T Mon	06 25 13.0	07 05 08.6	203.6	−2.6	16.1	1416	27.025	9.1	150	21.0	110	Yes
ζ Gem	07 04 06.5	20 34 13.1	195.8	11.9	−5.47	383	10.151	6.4	73	14.9	326	No
RS Pup	08 13 04.2	−34 34 42.7	252.4	−0.2	1.28	1543	41.388	9.9	214	20.8	318	No
X Cyg	20 43 24.2	+35 35 16.1	76.8	−4.3	26.42	981	16.386	7.5	105	52.5	248	No

Note. Units of R.A. are hours, minutes, and seconds. Units of decl. are degrees, arcminutes, and arcseconds. Explanation of columns: (1) star name; (2) and (3) R.A. and decl. (J2000.0); (4) and (5) Galactic coordinates; (6) systemic velocity relative to the Local Standard of Rest (LSR); (7) adopted distance in parsecs; (8) pulsation period in days; (9) mass, computed as $\log(M/M_\odot) = 0.297(\log L_\star/L_\odot) - 0.259$ where $L_\star$ is the stellar luminosity (Evans et al. 2013); (10) mean stellar radius, computed from the period-radius relation of Kervella et al. (2004); (11) space velocity, computed following Johnson & Soderblom (1987), adopting the solar constants from Schönrich et al. (2010) and the proper motions from van Leeuwen (2007); (12) position angle of space motion in the plane of the sky; (13) binary status. Coordinates were taken from SIMBAD (http://simbad.harvard.edu). Distances and pulsation periods were taken from Fernie et al. (1995). The luminosities used to compute the masses in column (9) are derived from $M_{V,\star} - M_{V,\odot} + \mathrm{BC} = -2.5\log(L_\star/L_\odot)$, where the solar absolute V magnitude is $M_{V,\odot} = 4.73$, the stellar absolute V magnitude is taken to be $M_{V,\star} = -4.04 - 2.43(\log P - 1.0)$ (Evans et al. 2013), and the bolometric corrections (BC) are from Flower (1996).

cases, there is evidence that a stellar wind has had a role in *shaping* the IR-emitting material. Similarly, Marengo et al. (2010a) suggested that near-IR emission seen close to the star may result from shocked gas emission rather than dust. Nonetheless, the presence of this emission is consistent with a pulsationally driven wind.

Another line of evidence for Cepheid mass loss comes from the work of Neilson et al. (2012b), who analyzed the observed rates of period change, $\dot{P}$, for a sample of 200 Galactic Cepheids and compared the results to stellar evolution models. They found that models without mass loss could not reproduce the observed $\dot{P}$ trends. However, mass loss on the Cepheid instability strip at a mean rate $\dot{M} \sim 10^{-7}\,M_\odot\,\mathrm{yr}^{-1}$ rectifies the models with observations. For the specific case of Polaris, Neilson et al. (2012a) concluded that a mass-loss rate of $\dot{M} \sim 10^{-6}\,M_\odot\,\mathrm{yr}^{-1}$ is necessary to account for the secular period change of this star over the past ∼200 yr.

Because of the moderate temperatures of Cepheids (∼5000–6000 K), their winds are expected to be predominantly neutral and atomic (Glassgold & Huggins 1983), with at most a modest ionized fraction (e.g., Engle et al. 2014). This makes the H I 21 cm line a potentially powerful tracer of Cepheid outflows. Although contamination from interstellar H I emission along the line-of-sight tends to be strong toward sources near the Galactic plane, the finite outflow velocity of the wind is expected in most cases to shift a portion of the circumstellar gas outside of the velocity range most strongly affected by line-of-sight emission. In addition, interferometers act as spatial filters against the largest scale components of the line-of-sight emission, which can aid in disentangling circumstellar signals from foreground and/or background signals (Bowers & Knapp 1987; Matthews & Reid 2007; Le Bertre et al. 2012).

Motivated by these factors, Matthews et al. (2012; hereafter M12) used the legacy Very Large Array (VLA) to observe δ Cep in the H I 21 cm line with the goal of searching for a gaseous counterpart to the stellar wind revealed by the *Spitzer* observations of Marengo et al. (2010b). Based on the H I data, M12 reported the discovery of an extended H I nebula (∼13′, or 1 pc across), surrounding the position of δ Cep. This nebula exhibits a head–tail morphology, consistent with debris that was ejected from the star and subsequently sculpted by its interaction with the interstellar medium (ISM). M12 derived an outflow velocity for the wind of $V_o \approx 35.6 \pm 1.2\,\mathrm{km\,s}^{-1}$—the first ever directly measured from a Cepheid—and constrained the mass-loss rate to be $\dot{M} \approx (1.0 \pm 0.8) \times 10^{-6}\,M_\odot\,\mathrm{yr}^{-1}$.

If similar H I envelopes are present around other Cepheids, this would have profound implications for our understanding of these stars and our ability to constrain their mass-loss and evolutionary histories. For this reason, we have undertaken H I imaging observations of a sample of four additional Galactic Cepheids using the upgraded Karl F. Jansky VLA of the National Radio Astronomy Observatory.[4] As described below, these observations have uncovered evidence for circumstellar material associated with one additional Cepheid and allow us to place limits on the mass of circumstellar material associated with the three remaining targets.

2. TARGET SELECTION

A sample of four Galactic Cepheids was targeted in the present study : RS Puppis (RS Pup), T Monocerotis (T Mon), X Cygni (X Cyg), and ζ Geminorum (ζ Gem). Some of their properties are summarized in Table 1.

The long-period Cepheid RS Pup is one of the brightest known Cepheids in the Galaxy. Based on its rate of period change it is thought to be on its third crossing of the instability strip (Berdnikov et al. 2009). This star is unique among Galactic Cepheids in being surrounded by an extended (∼2′ across) optical reflection nebula (Westerlund 1961). This nebula is also visible in the IR (e.g., McAlary & Welch 1986), including the multi-band *Spitzer* observations presented by Kervella et al. (2009) and Barmby et al. (2011). Although it was suggested early-on that the RS Pup nebula may be the result of mass loss (either during the Cepheid phase or a previous red giant stage; Havlen 1972), Kervella et al. (2009, 2012) argued that the bulk of the nebula instead comprises cold, dusty interstellar material (see also Deasy 1988; Barmby et al. 2011) that was shaped and compressed by a stellar wind or outflow, possibly during an earlier evolutionary phase as a rapidly rotating B dwarf. However, Kervella et al. (2009) also detected evidence of a warm emission component toward RS Pup at 10 μm, with spatial scales of ∼100–1000 AU. This latter component is interpreted as a

[4] The National Radio Astronomy Observatory is operated by Associated Universities, Inc., under cooperative agreement with the National Science Foundation.

hallmark of ongoing Cepheid-phase mass loss (see also Gallenne et al. 2011).

Among the remaining stars in the Barmby et al. (2011) sample that showed either clear or possible extended emission, only two are far enough north to observe with VLA: T Mon and X Cyg. Both of these stars show extended emission at 8.0 μm, but only tentative detections at 24 μm and/or 70 μm.

X Cyg is one of the most luminous classical Cepheids visible from the Northern Hemisphere and is believed to be on its third crossing of the instability strip (Turner 1999). Observations to date provide no compelling evidence for a companion (Evans 1984, 1992; Turner 1998), although a low-mass companion with an orbit in the plane of the sky cannot be excluded. T Mon, on the other hand, is a well-known binary (Mariska et al. 1980; Coulson 1983) with an orbital period between 90 and 260 yr (Evans et al. 1999). The companion is a hot, chemically peculiar A star that is itself most likely a binary in a short-period orbit. T Mon was studied by Gallenne et al. (2013) using mid-IR interferometry, and these authors detected a mid-IR excess that they attributed to the presence of a CSE.

In contrast to the other three stars in Table 1, our fourth target, ζ Gem, does not exhibit any extended IR emission in the study of Barmby et al. (2011). This medium-period Cepheid was included in the present sample in part to test whether observable signatures of mass loss are exclusive to stars with extended IR emission. In addition, this star was predicted to have minimal line-of-sight H I contamination because of the low cirrus levels seen in the images of Barmby et al. and the modest H I brightness temperatures along this direction seen in previous H I survey data. Based on its declining period (Berdnikov et al. 2000), ζ Gem is believed to be on its second crossing of the instability strip (e.g., Turner et al. 2006).

To provide context for the interpretation of our VLA results and to illustrate the strength and velocity extent of the line-of-sight confusion toward each of our targets, we show in Figure 1 H I spectra toward each stellar position (to within the nearest $0\overset{\circ}{.}2$) extracted from the Leiden Argentine Bonn (LAB) all-sky H I survey (Kalberla et al. 2005). Because the LAB spectra were obtained with single-dish telescopes, they are not affected by filtering of large-scale emission (i.e., missing short spacing information) and directly measure the total beam-integrated H I flux. Note, however, that the noise level in the LAB spectra (~0.6 Jy rms) precludes the detection of typical weak circumstellar signals, even outside of the velocity ranges affected by interstellar contamination.

3. OBSERVATIONS AND DATA REDUCTION

H I 21 cm line observations of each of our target stars were carried out with the VLA in late 2011 and early 2012 (Table 2). To obtain maximum sensitivity to extended emission, the most compact (D) configuration was used for X Cyg, T Mon, and ζ Gem (with baselines ranging from 0.035–1.03 km) and the hybrid DnC configuration (0.035–1.6 km baselines) was used for the southern source RS Pup. These configurations provide sensitivity to emission on angular scales of up to ~16′. The primary beam of the VLA at our observing frequency is ~31′. During each observing session, observations of the target star were interspersed with observations of a neighboring bright point source to provide calibration of the complex gains. Additionally, either 3C48 or 3C286 was observed as an absolute flux density calibrator and bandpass calibrator (see Table 2).

The WIDAR correlator was configured with eight subbands across each of two basebands, both of which measured dual circular polarizations. Because the two basebands sample the same data stream, averaging them does not improve the rms noise, hence only data from the first baseband pair (A0/C0) were used for the present analysis. Each of the subbands had a bandwidth of 0.25 MHz with 128 spectral channels, providing a channel spacing of 1.95 kHz (~0.41 km s^{-1}). The eight subbands were tuned to contiguously cover a total bandwidth of 2 MHz.

The data for each target star were taken with the central baseband frequency tuned to approximately match the LSR velocity of the star (see Tables 1 and 2). However, additional observations of the phase and bandpass calibrators were made with the frequency center shifted by $\sim\pm$1.5–2 MHz, respectively (see Table 3). The offsets adopted for each case were determined based on the velocity distribution of the Galactic H I in the neighborhood of the star, as determined using spectra from Kalberla et al. (2005). This approach mitigated contamination from Galactic H I emission in the band and thus permitted a more robust bandpass calibration and more accurate bootstrapping of the flux density scale.

All data processing was performed using the Astronomical Image Processing System (AIPS; Greisen 2003). Data were loaded into AIPS from archival science data model format files using the BDFIn program from the Obit software package (Cotton 2008). This step enables the creation of tables containing on-line flags and system power measurements. Data for RS Pup were taken with 5 s integrations times, while data for the other three stars were recorded with 1 s integration times, but averaged to 5 s time resolution in post-processing, prior to beginning the calibration.

After updating the antenna positions to the best available values and flagging obviously corrupted data, an initial calibration of the visibility data was performed using the AIPS task TYAPL, which uses the system power measurements to compute data weights (Perley 2010). Calibration of the bandpass and the frequency-independent portion of the complex gains was subsequently performed using standard techniques, taking into account the special considerations for recent VLA data detailed in Appendix E of the AIPS Cookbook.[5] In addition, the gain solutions for subbands affected by contamination from line emission were interpolated from the adjacent subbands when necessary. Following these steps, time-dependent frequency shifts were applied to the data to compensate for the Earth's motion, and the data were Hanning smoothed in frequency, dropping every other spectral channel. The resulting velocity resolution is ~0.82 km s^{-1}. For stars observed during multiple non-contiguous sessions, the data from the different sessions were concatenated following this step.

Prior to imaging the line data, continuum emission in the field was subtracted using either a linear fit to the real and imaginary components of the visibilities via the AIPS task UVLIN, and/or subtraction of a clean component model of the continuum (via the AIPS task UVSUB). The portions of the band that were determined to be line-free and were used to define the continuum are summarized in Column 8 of Table 4.

An image of the 21 cm continuum emission in the field of each target star was produced from the line-free portion of the band using the Clean deconvolution algorithm as

[5] http://www.aips.nrao.edu/cook.html

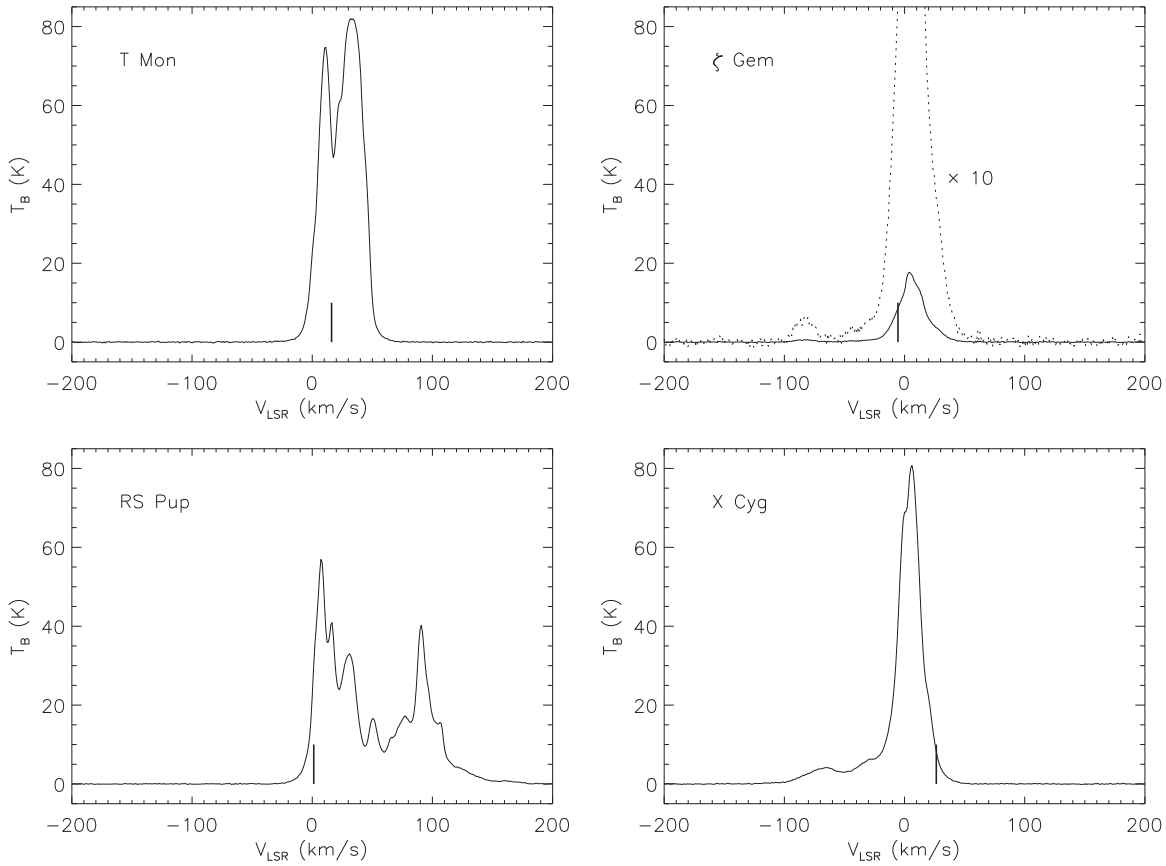

Figure 1. Leiden/Argentine/Bonn (LAB) single-dish H I spectra (Kalberla et al. 2005) toward each of the Cepheids observed with the VLA, illustrating the line-of-sight interstellar emission. Each spectrum shows brightness temperature in kelvin plotted as a function of LSR velocity in km s^{-1}. For ζ Gem, the dotted line shows the original spectrum multiplied by a factor of 10. Vertical bars indicate the stellar systemic velocity.

Table 2
Summary of VLA Observations

Star	Obs. Date	V_{cent} (km s^{-1})	V_{min}, V_{max} (km s^{-1})	No. antennas	t (hr)	Config.
(1)	(2)	(3)	(4)	(5)	(6)	(7)
ζ Gem	2011 Dec 03	−5.5	−215.7, 205.6	27	2.75	D
ζ Gem	2011 Dec 04	−5.5	−215.7, 205.6	27	2.75	D
X Cyg	2011 Dec 04	26.4	−183.8, 237.5	26	2.94	D
X Cyg	2011 Dec 05	26.4	−183.8, 237.5	26	2.93	D
T Mon	2011 Dec 05	15.6	−194.7, 226.6	25	2.86	D
RS Pup	2012 Jan 16	1.3	−209.0, 212.3	25	1.90	DnC
RS Pup	2012 Jan 17	1.3	−209.0, 212.3	25	1.90	DnC
RS Pup	2012 Jan 21	1.3	−209.0, 212.3	24	1.90	DnC

Note. Explanation of columns: (1) star name; (2) date of observation; (3) LSR velocity at band center; (4) minimum and maximum LSR velocity covered by the observing band; (5) number of available antennas; (6) total on-source integration time; (7) antenna configuration.

implemented in the AIPS task IMAGR (see Table 4). The peak continuum flux densities measured within the primary beam for each of the target fields were as follows: 15.6 mJy (ζ Gem); 30.2 mJy (T Mon); 53.4 mJy (RS Pup); 15.1 mJy (X Cyg). No continuum emission was detected coincident with any of the target stars.

Deconvolved image cubes of the H I line emission were also produced using IMAGR. For each target, data cubes were produced using various weighting schemes for the visibilities. The characteristics of the data cubes used for the present analysis are summarized in Table 4.

4. OBSERVATIONAL RESULTS

Consistent with the single-dish spectra shown in Figure 1, the interpretation of the H I data for all of our Cepheid targets is impacted over portions of the observing band by the presence of strong interstellar H I emission along the line-of-sight. In general, this emission contains large-scale components (>15′) that are poorly sampled by the VLA D configuration. Consequently, the true spatial structure of the gas over the affected velocity ranges cannot be fully reconstructed in our deconvolved images, leading to characteristic artifacts, including patterns of strong positive and negative components that fill

Table 3
Calibration Sources

Source	α(J2000.0)	δ(J2000.0)	Flux Density (Jy)	ν_0 (GHz)	Date
3C48[a]	01 37 41.2994	+33 09 35.133	16.2632[b]	1.4194	2011 Dec 04 and 05
	...	...	16.2627[b]	1.4193	2011 Dec 05
J0632+1022[c]	06 32 15.3269	10 22 01.676	2.377 ± 0.010	1.4198	2011 Dec 05
J0738+1742[d]	07 38 07.3937	17 42 18.998	0.962 ± 0.009	1.4204	2011 Dec 03
	...	...	0.970 ± 0.018	1.4204	2011 Dec 04
J0828-3731[e]	08 28 04.7803	−37 31 06.281	1.894 ± 0.008	1.4203	2012 Jan 16
	...	...	1.898 ± 0.010	1.4203	2012 Jan 17
	...	...	1.885 ± 0.011	1.4203	2012 Jan 21
3C286[f]	13 31 08.2879	+30 30 32.958	15.0515[b]	1.4196	2011 Dec 03
	...	...	15.0515[b]	1.4196	2011 Dec 04
	...	...	15.0520[b]	1.4195	2012 Jan 16
	...	...	15.0520[b]	1.4195	2012 Jan 17
	...	...	15.0521[b]	1.4195	2012 Jan 21
J2052+3635[g]	20 52 52.0550	+36 35 35.300	4.913 ± 0.028	1.4205	2011 Dec 04 and 05

Notes. Units of R.A. are hours, minutes, and seconds, and units of decl. are degrees, arcminutes, and arcseconds. ν_0 is the frequency at which the flux density in the fourth column was computed.
[a] Primary flux calibrator and bandpass calibrator for X Cyg and T Mon.
[b] Flux densities were determined using the time-dependent coefficients from Perley & Butler (2013). For 3C48, the flux density S_ν as a function of frequency was taken to be $\log(S_\nu) = 1.3322 - 0.7688(\log(\nu)) - 0.1952(\log(\nu))^2 + 0.0593(\log(\nu))^3$, where $\nu_{\rm GHz}$ is the frequency expressed in GHz. For 3C286, $\log(S_\nu) = 1.2515 - 0.4605(\log(\nu)) - 0.1715(\log(\nu))^2 + 0.0336(\log(\nu))^3$.
[c] Secondary gain calibrator for T Mon.
[d] Secondary gain calibrator for ζ Gem.
[e] Secondary gain calibrator for RS Pup.
[f] Primary flux calibrator and bandpass calibrator for RS Pup and ζ Gem.
[g] Secondary gain calibrator for X Cyg.

Table 4
Deconvolved Image Characteristics

Source	Type	$\mathcal{R}$	Taper (kλ, kλ)	$\theta_{\rm FWHM}$ ($'' \times ''$)	PA (°)	$\sigma_{\rm rms}$ (mJy beam^{-1})	Continuum Channels	Clean Boxes?
(1)	(2)	(3)	(4)	(5)	(6)	(7)	(8)	(9)
X Cyg	cont.	1	...	52.″2 × 49.″8	−78.4	0.19	8–228; 411–500	Yes
X Cyg	line	5	...	58.″8 × 55.″7	−70.6	1.2	8–228; 411–500	No
X Cyg	line	5	2, 2	96.″8 × 93.″0	−39.6	1.4	8–228; 411–500	No
RS Pup	cont.	1	...	49.″0 × 40.″8	27.2	0.14	1–45; 290–512	Yes
RS Pup	line	5	...	55.″3 × 44.″4	27.2	1.4	1–45; 290–512	No
RS Pup	line	5	4, 4	68.″7 × 55.″2	13.7	1.5	1–45; 290–512	No
ζ Gem	cont.	1	...	48.″8 × 45.″4	−9.8	0.10	10–196; 280–230; 370–502	Yes
ζ Gem	line	5	...	55.″3 × 50.″2	−14.1	1.1	10–196; 280–230; 370–502	No
ζ Gem	line	5	2, 2	96.″5 × 87.″5	−24.6	1.3	10–196; 280–230; 370–502	No
T Mon	cont.	1	...	60.″0 × 45.″6	−3.1	0.15	1–185; 330–512	Yes
T Mon	line	5	...	69.″8 × 48.″8	−2.5	1.5	10–185; 330–500	Yes
T Mon	line	5	2, 2	109.″3 × 85.″5	−10.1	1.8	10–185; 330–500	Yes

Note. Explanation of columns: (1) target name; (2) indication of whether the image contains line or continuum emission; the continuum images comprise a single spectral channel representing an average of the line-free portions of the band; (3) AIPS robust parameter used in image deconvolution; $\mathcal{R} = +5$ is comparable to natural weighting; (4) Gaussian taper applied in u and v directions, expressed as distance to 30% point of Gaussian in units of kilolambda; (5) FWHM dimensions of synthesized beam; (6) position angle of synthesized beam (measured east from north); (7) rms noise per channel (1σ); (8) spectral channels used for continuum subtraction (line data) or that were averaged to compute a continuum image; (9) indication of whether or not clean boxes were used during image deconvolution.

the field-of-view (cf. Figure 1 of M12 and Figure 3 discussed below). In the discussion that follows, we designate a spectral channel as likely to be contaminated by Galactic emission if its noise characteristics in a deconvolved data cube exhibit an excess of both positive and negative pixels at a significance of $>3\sigma$ compared with what is expected from a Gaussian noise distribution. Because of the spatial filtering effects of an interferometer, not all of the velocities containing line-of-sight emission in the single-dish spectra in Figure 1 contain discernible contamination in the VLA maps, but in general, the single-dish spectra are a good predictor of which velocity ranges will be impacted.

4.1. T Monocerotis (T Mon)

Along the line-of-sight to T Mon, the stellar systemic velocity ($V_{\star,\rm LSR} = 16.1\,{\rm km\,s^{-1}}$) is coincident with strong interstellar foreground/background emission. Consistent with the LAB spectrum shown in Figure 1, we find that the VLA H I channel images for T Mon are affected by moderate to strong

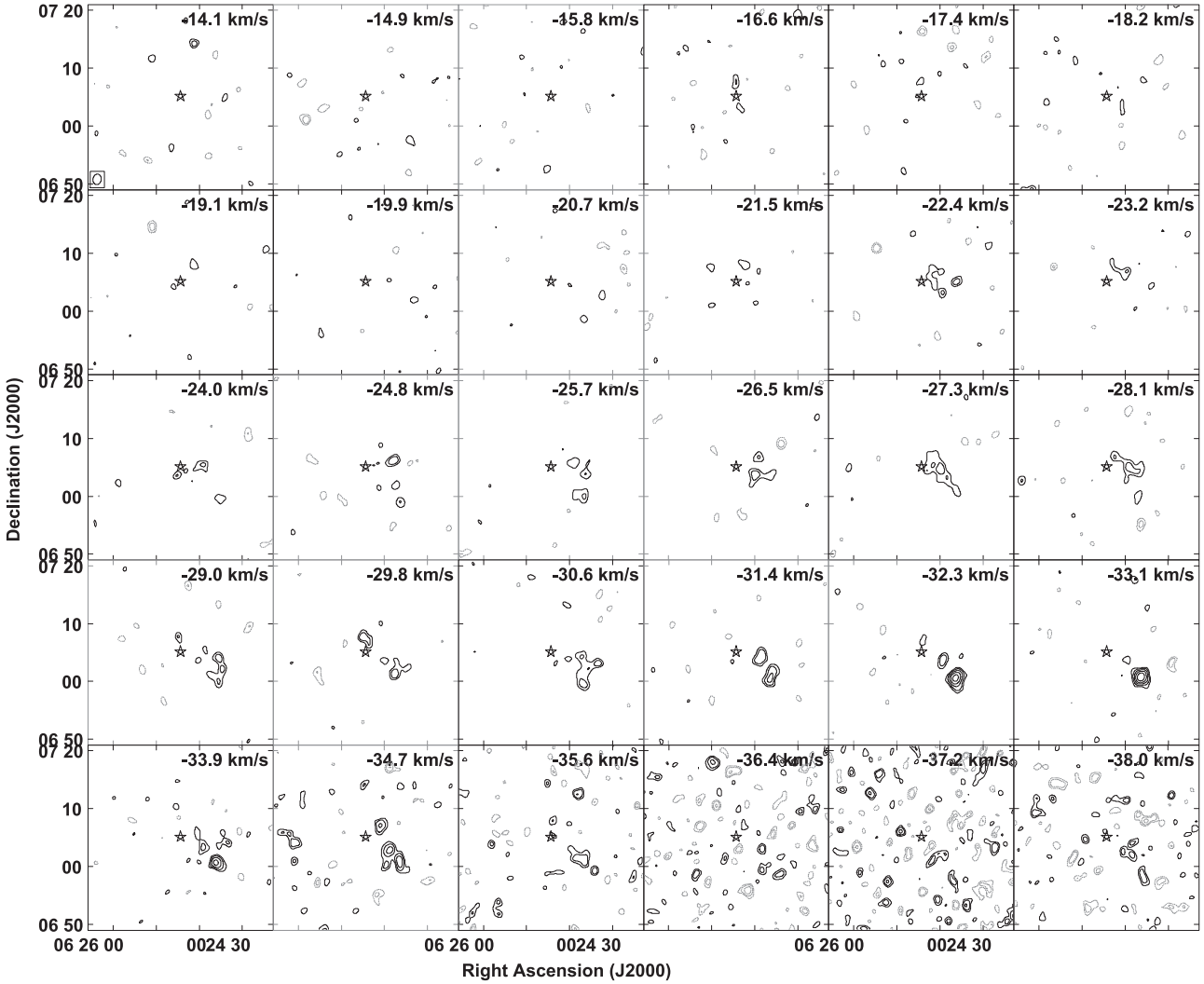

Figure 2. H I channel maps toward T Mon, derived from a tapered version of the VLA data. The channels shown are blueshifted from the stellar systemic velocity of $V_{\star,\mathrm{LSR}} = 16.1\ \mathrm{km\ s^{-1}}$. A star symbol marks the stellar position. Contour levels are -12, -8.5, -6, -4.2, -3, 3, …12) $\times$ 1.8 mJy beam^{-1}, where the lowest contour level is $\sim 3\sigma$. Negative contours are shown as gray dotted lines; positive contours are plotted in black. The higher rms noise in channels between -24.7 and $-38.8\ \mathrm{km\ s^{-1}}$ results from aliased noise at the subband edges in the WIDAR correlator. The size of the synthesized beam ($109'' \times 85''$) is indicated in the lower left corner of the first panel.

line-of-sight confusion over the velocity range $-13.3 \lesssim V_{\mathrm{LSR}} \lesssim 64.2\ \mathrm{km\ s^{-1}}$. We therefore focus our search for circumstellar emission outside of this window.

In Figure 2 we present H I channel maps for a range of velocities blueshifted by $\sim$30–54 km s^{-1} from the stellar systemic velocity. Within the first few channels shown (which are closest in velocity to the dominant Galactic emission), no obvious signs of large-scale Galactic contamination are apparent, and the noise is consistent with thermal noise. In the bottom row of Figure 2, the elevated noise in several channels results from aliased noise at the subband edges of the WIDAR correlator. However, in between, we find signatures of spatially extended emission that are visible at or near the stellar position over several contiguous channels with a significance of $\geqslant 3\sigma$.

Figure 3 shows a series of channels images redshifted from the stellar velocity. A few of these channels also show possible hints of extended emission feature near the position of the star, although they are weaker than the features seen at comparable velocity offsets on the blue side of the stellar systemic velocity, and in general the identification of genuine features redward of $V_{\star,\mathrm{sys}}$ is hindered by aliased noise at the subband edges (affecting velocities 66.7–70.8 km s^{-1}) and by line-of-sight contamination (which affects velocities $V_{\mathrm{LSR}} \lesssim 64.2\ \mathrm{km\ s^{-1}}$).

To further illustrate the nature of the emission visible in Figures 2 and 3, we show in Figure 4 an H I total intensity map derived from these data. This zeroth moment map was produced using emission between velocities -33.9 and 65.9 km s^{-1}. Channels between -13.2 and 64.2 km s^{-1}, which are clearly dominated by Galactic contamination, were blanked, and a cutoff of 1.8 mJy beam^{-1} (1σ) was imposed after smoothing the data with a Hanning function in frequency and a Gaussian kernel with a FWHM of 7 pixels ($70''$) spatially.

Figure 4 reveals what appears to be a partial shell-like structure several arcminutes across. At the distance of T Mon, the projected extent of the structure corresponds to $\sim$2 pc. The bulk of the emission is offset to the northwest of the star, with only marginal evidence of emission extending across the position of T Mon itself. However, it is interesting to note that the offset between putative shell and T Mon lies along the space trajectory of the star, indicated by an arrow on Figure 4. This space velocity vector was computed using the distance

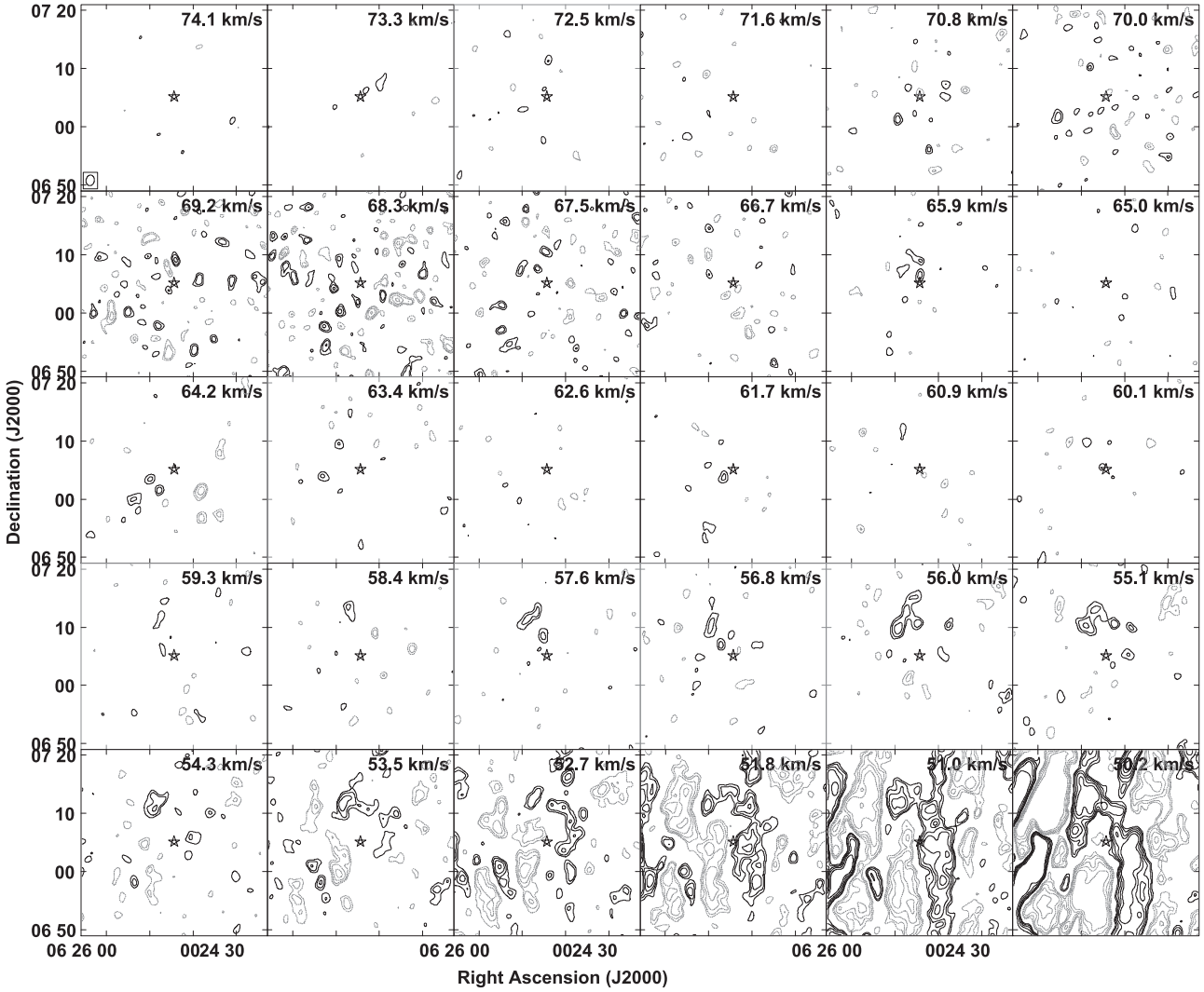

Figure 3. As in Figure 2, but for velocities redshifted from the systemic velocity of T Mon. Channels in the bottom row are dominated by large-scale Galactic emission along the line-of-sight. The elevated noise in channels from 66.7 to 70.0 km s^{-1} results from aliasing at the subband boundaries in the WIDAR correlator.

and systemic velocity from Table 1 and the proper motion for T Mon from van Leeuwen (2007); it corresponds to a 3D velocity of 21.0 km s^{-1} along a position angle of 110°. Another noteworthy feature is that in the direction trailing the arrow, roughly 2′ behind the star (corresponding to a projected distance of ∼0.82 pc), there appears to be a depression or cavity in the H I nebula. Together these features raise the intriguing possibility that the observed H I emission corresponds to material shed during an earlier epoch of mass loss from T Mon (see Section 5 for discussion).

Based on an examination of the channel maps in Figure 2, the knot of emission visible to the southwest of the putative shell (i.e., near $\alpha_{J2000} = 06^h24^m49\overset{s}{.}6$, $\delta_{J2000} = 07°00' 41\overset{''}{.}0$) appears to be spatially and spectrally distinct from the remainder of the nebula and is therefore likely to be unrelated. The line profile of this knot peaks near $V_{LSR} \approx -33.1$ km s^{-1} with a FWHM of 3.7 ± 2.2 km s^{-1}, and is therefore blueshifted relative to the bulk of the emission in the main nebula. Excluding this knot, the dimensions of the remainder of the nebula are approximately $6\overset{'}{.}1 \times 4\overset{'}{.}5$ (∼2.6 × 2.0 pc at the distance of T Mon).

To illustrate the spectral characteristics of the emission in the vicinity of T Mon, we plot in the upper panel of Figure 5 a spectrum integrated over a rectangular region encompassing the nebula visible in Figure 4 with exception of the southwestern knot. (A spectrum toward the knot is overplotted as a gray dotted line for comparison.) The aperture spanned $6\overset{'}{.}2$ east–west and $8\overset{'}{.}2$ north–south, and was centered at $\alpha_{J2000} = 06^h\ 25^m\ 05\overset{s}{.}6$, $\delta_{J2000} = 07°04'58\overset{''}{.}6$.

Outside of the velocity range dominated by Galactic emission (designated by a blue line on Figure 5), we see evidence of an emission peak offset to the blue of the stellar systemic velocity by ∼45 km s^{-1}. There is also marginal evidence for a much weaker redshifted peak at ∼50 km s^{-1} from $V_{\star,sys}$.

In the H I total intensity image shown in Figure 5, H I emission is only marginally detected at the position of T Mon itself. Consistent with this, a spectrum integrated over a single synthesized beam centered on the star shows no significant emission outside the spectral regions affected by confusion (lower panel of Figure 5).

To estimate the total quantity of gas associated with the nebula in Figure 4, we use the spectrum plotted in the upper panel of Figure 5. Integrating over the same velocity ranges used to derive the H I total intensity map (and similarly excluding the portion of the spectrum deemed contaminated

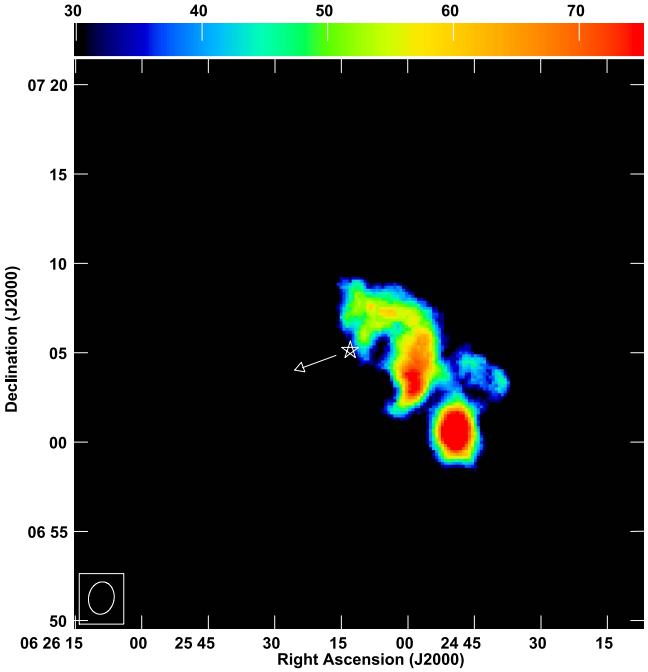

Figure 4. H I total intensity map of the region surrounding T Mon, derived from a tapered data cube. The map incorporates emission over velocities $-33.9 \leqslant V_{\rm LSR} < -13.2$ km s^{-1} and $64.2 < V_{\rm LSR} \leqslant 65.9$ km s^{-1}. Spectral channels between -13.2 and 64.2 km s^{-1} were excluded owing to contamination from line-of-sight emission. A cutoff of 1.8 mJy beam^{-1} (1σ) was imposed after smoothing the data with a Hanning function in frequency and a boxcar kernel with a FWHM of 7 pixels (70″) spatially. Intensity levels are in units of Jy beam^{-1} m s^{-1}. The synthesized beam (109″ × 85″) is shown in the lower left corner. A star symbol indicates the position of T Mon, and the arrow indicates the direction of space motion of the star.

by interstellar emission), we find a velocity-integrated H I flux density of $\int SdV \sim 0.76$ Jy km s^{-1}. Assuming that the emission is optically thin, this translates to an H I mass of $M_{\rm HI} \approx 0.36 M_{\odot}$ at the distance of the star (see Section 6.1). This should be considered a lower limit to the total H I mass given the range of velocities that was excluded because of confusion. Applying a scaling factor of 1.4 to correct for the mass of helium, this translates to a total nebula mass of $\gtrsim 0.5 M_{\odot}$.

4.2. ζ Geminorum (ζ Gem)

As seen in Figure 1, the line-of-sight H I emission in the direction of ζ Gem is much weaker and narrower in velocity extent compared to the other three stars in the present sample. However, despite the modest confusion, we do not identify any statistically significant line emission in our H I data cubes that can be attributed to circumstellar gas.

In Figure 6 we plot two H I spectra toward the position of ζ Gem derived from our VLA data. The top panel shows a spectrum integrated over a 1 pc^2 box (536″ × 536″) centered on the star, while the lower panel shows a spectrum averaged over a single synthesized beam at the stellar position. No significant spectral features are detected in either spectrum outside of the velocity range that is dominated by line-of-sight confusion (indicated by blue horizontal lines), with the possible exception of near velocities ∼40–45 km s^{-1} in the spatially integrated spectrum. However, the H I channel maps (not shown) do not reveal any corresponding emission regions with a significance of $>3\sigma$. The features in both spectra near -83 km s^{-1} are clearly interstellar in nature; there is a counterpart in the LAB data (Figure 1), and the associated channel maps contain large-scale emission that fills the primary beam. In Section 6.1 we discuss upper limits to the circumstellar H I mass and mass-loss rate of ζ Gem based on these results.

4.3. RS Puppis (RS Pup)

As noted in Section 2, Kervella et al. (2009) reported evidence for a warm stellar wind from RS Pup based on near-IR interferometry observations. Our H I 21 cm line observations now permit a search for a gaseous counterpart to this wind, as well as for more spatially extended circumstellar material to which near-IR interferometry is insensitive. In addition, our VLA data allow a search atomic hydrogen associated with the RS Pup reflection nebula. As discussed in Section 2, the extended reflection nebula surrounding RS Pup is thought to comprise predominantly swept-up interstellar matter rather than circumstellar ejecta. Nonetheless, this nebula is believed to be physically associated with the star, and its cold temperature (≈40–45 K; McAlary & Welch 1986; Kervella et al. 2009; Barmby et al. 2011) make it a candidate for the presence of associated H I gas.

The LAB spectrum shown in Figure 1 reveals that strong interstellar H I emission is present over a wide range of velocities along the direction toward RS Pup. Correspondingly, our VLA channel images are contaminated by line-of-sight emission over a significant fraction of the observing band ($-25 \lesssim V_{\rm LSR} \lesssim 171$ km s^{-1}). This range encompasses the stellar systemic velocity ($V_{\star,\rm LSR} = 1.3$ km s^{-1}).

To illustrate the spectral characteristics of the H I emission near the position of RS Pup, we present in Figure 7 integrated H I spectra derived from our VLA data. The top panel shows the emission integrated over a 1 pc^2 (136″ × 136″) box centered on the star, while the lower panel shows a spectrum integrated over a single synthesized beam centered on the stellar position. The former region is roughly comparable in extent to the 70 μm emission nebula detected by *Spitzer* (cf. Barmby et al. 2011, their Figure 5).

Blueward of $V_{\rm LSR} \approx -25$ km s^{-1}, the Galactic emission toward RS Pup becomes negligible, providing a clean window for identification of possible circumstellar emission. However, we find no statistically significant emission near the position of RS Pup either in our H I channel maps (not shown) or in our integrated spectra. Over the total angular extent of the reflection nebula (∼4′; Kervella et al. 2012), spatial filtering of emission by VLA should not be a factor (see Section 3). We conclude that any atomic hydrogen associated with mass loss from RS Pup or with the RS Pup reflection nebula is either below our detection threshold or lies at velocities affected by confusion from line-of-sight emission. In Section 6.1 we use these results to estimate upper limits to the circumstellar H I mass and mass-loss rate of RS Pup.

4.4. X Cygnus (X Cyg)

In the direction of X Cyg, our VLA H I channel maps over the velocity range $-100 \lesssim V_{\rm LSR} \lesssim 45$ km s^{-1} contain the hallmarks of contamination from line-of-sight emission. Consistent with this, the LAB spectrum toward the position of X Cyg (Figure 1) shows the presence of strong interstellar emission over this velocity range. In contrast, for velocities $V_{\rm LSR} \gtrsim 45$ km s^{-1}, the LAB spectrum toward X Cyg appears

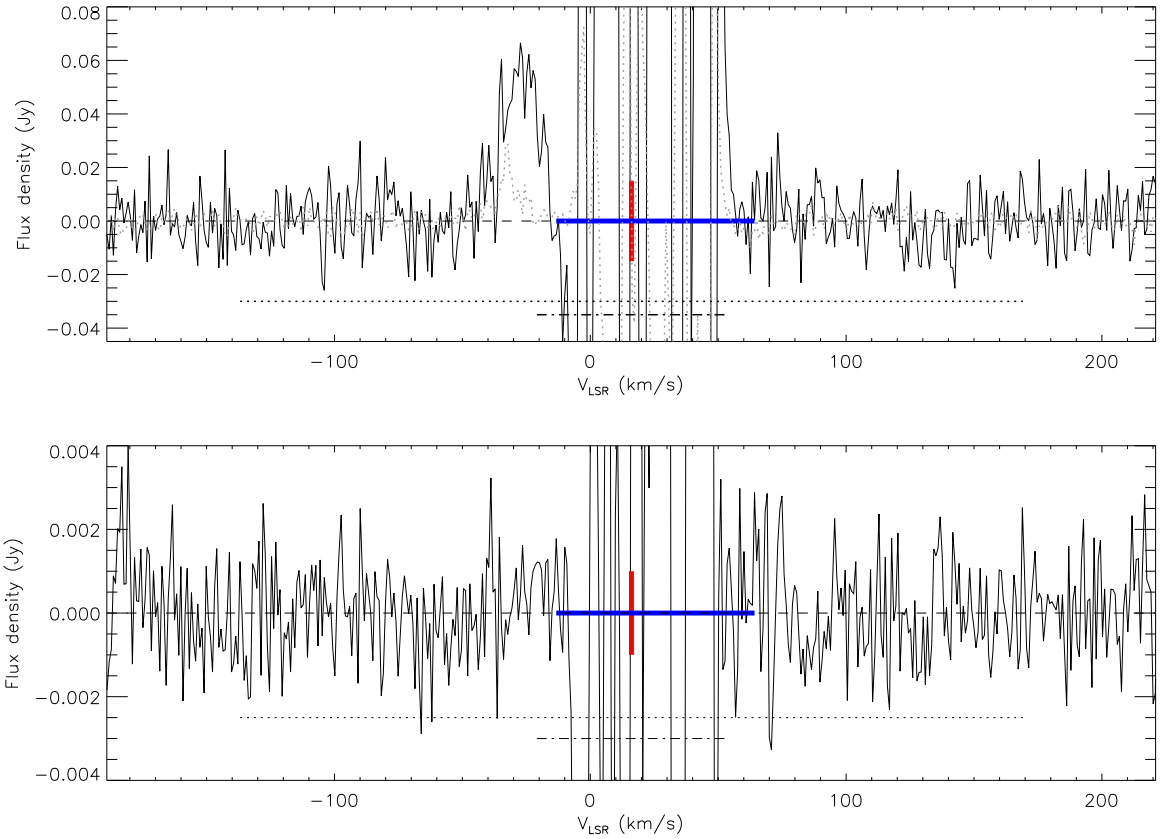

Figure 5. VLA H I spectra in the neighborhood of T Mon, derived from naturally weighted data after correction for the primary beam. Top: the black solid line shows a spectrum integrated over a box with dimensions 6.′2 east–west and 8.′2 north–south, centered on the emission nebula visible in Figure 4. This aperture excludes the emission knot to the southwest. A spectrum toward the emission knot itself is overplotted as a gray dotted line. Bottom: spectrum integrated over a single synthesized beam, centered on T Mon. In both spectra, the red vertical lines indicate the stellar systemic velocity and the blue horizontal lines denote the velocity ranges over which analysis of the VLA data is impeded by contamination from interstellar emission along the line-of-sight (see Figure 1). The horizontal dotted lines indicate twice the escape velocity from the stellar surface, and the horizontal dot-dashed lines indicate the predicted linewidth if the outflow obeys Reimers' (1977) formula (see Section 6.1).

virtually free of contaminating emission, providing a relatively clean spectral window to search for circumstellar emission redshifted from the stellar systemic velocity of $V_{\star,\mathrm{LSR}} = 26.4\,\mathrm{km\,s^{-1}}$. However, based on inspection of our H I data cubes, we find no statistically significant emission at or near the stellar position over the velocity range $45 \lesssim V_{\mathrm{LSR}} \lesssim 237\,\mathrm{km\,s^{-1}}$. Similarly, spectra derived by summing the emission over a 1 pc^2 ($210'' \times 210''$) box surrounding the star (Figure 8, top) or a single synthesized beam centered on the star (Figure 8, bottom) reveal no signs of significant spectral features outside the velocity range that is contaminated by line-of-sight confusion. We discuss upper limits on the circumstellar H I mass and mass-loss rate of X Cyg in Section 6.1.

5. T MON: AN H I NEBULA ASSOCIATED WITH PREVIOUS MASS LOSS?

While a chance superposition of an unrelated gas cloud along the line-of-sight cannot be entirely excluded as an explanation for the "shell" of emission seen near T Mon (Figure 4), several characteristics of this emission are consistent with a possible association with the star. We now discuss these arguments in more depth, and consider the implications for the evolutionary history of T Mon if this shell is indeed associated with stellar mass loss.

5.1. Implications of the Shell Morphology and Kinematics on Its Probable Origin

It is now well established that detectable circumstellar envelopes of atomic hydrogen, spanning up to a parsec or more in size, form around certain types of evolved, mass-losing stars, and furthermore that the properties of these envelopes are significantly impacted by the space motion of the stars and the interaction of the stellar ejecta with the ISM (e.g., Gérard & Le Bertre 2006; Le Bertre et al. 2012; Matthews et al. 2013). For stars with low space velocities, quasi-spherical shells may be observed, while in cases where the space velocity is sufficiently high, bow shocks may be detectable in IR and ultraviolet wavelengths, and the effects of ram pressure may sweep back a portion of the ejecta to form a trailing gaseous wake (see M12; Matthews et al. 2013 and references therein). Numerical models also predict that the properties of the shells will change significantly as stars evolve and undergo changes in their mass-loss rates, and as the ejecta expand into the ISM (e.g., Wareing et al. 2007; Villaver et al. 2012). However, one general consequence of the central star's space motion will be an eventual shift of the star from the geometric center of the shell to a position nearer its leading edge (e.g., Smith 1976). Once the mass loss wanes, the star will eventually completely exit the nebula (Smith 1976; Wareing et al. 2007) and leave only a partial shell downstream (see Figure 7(d) of Wareing et al.).

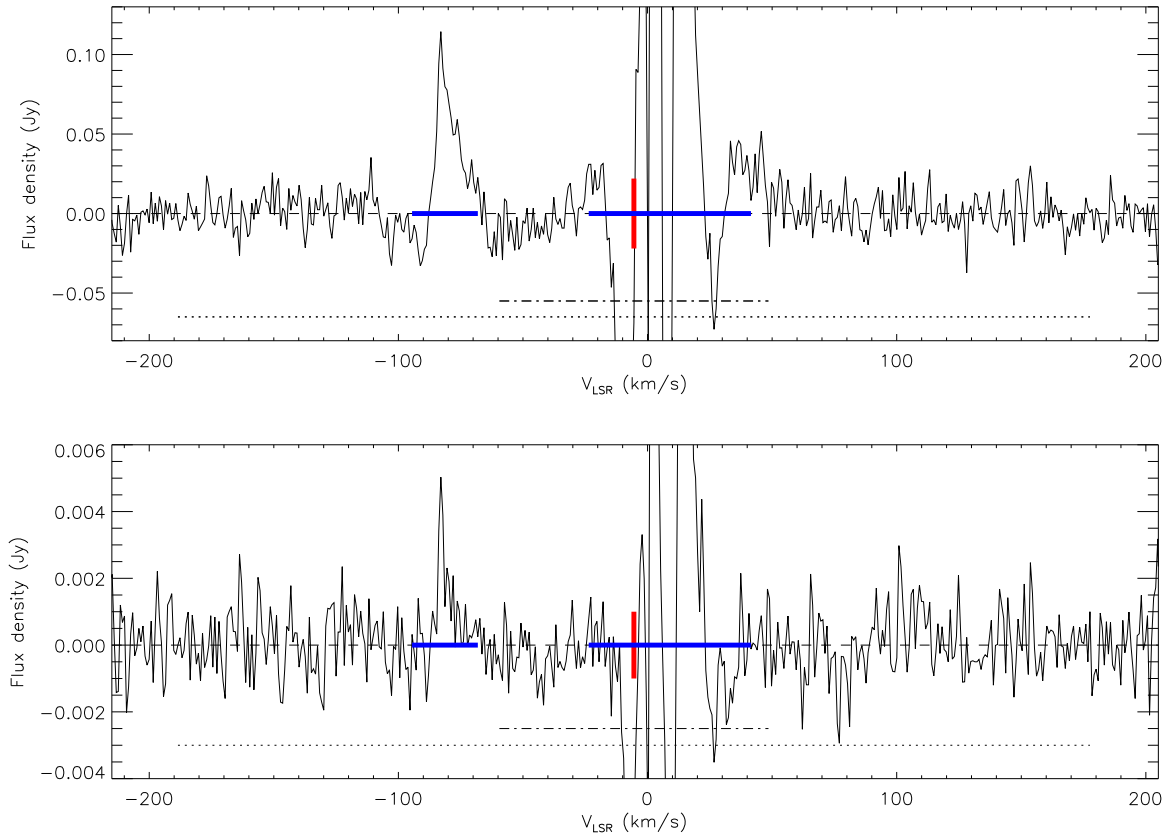

Figure 6. Top: VLA H I spectrum toward ζ Gem, derived from a naturally weighted data cube by integrating over a $\sim$1 $\times$ 1 pc box (538″ $\times$ 538″) surrounding ζ Gem. The data are corrected for the VLA primary beam. Bottom: H I spectrum integrated over a single synthesized beam centered on the star. The meanings of the overplotted vertical and horizontal lines are as in Figure 5.

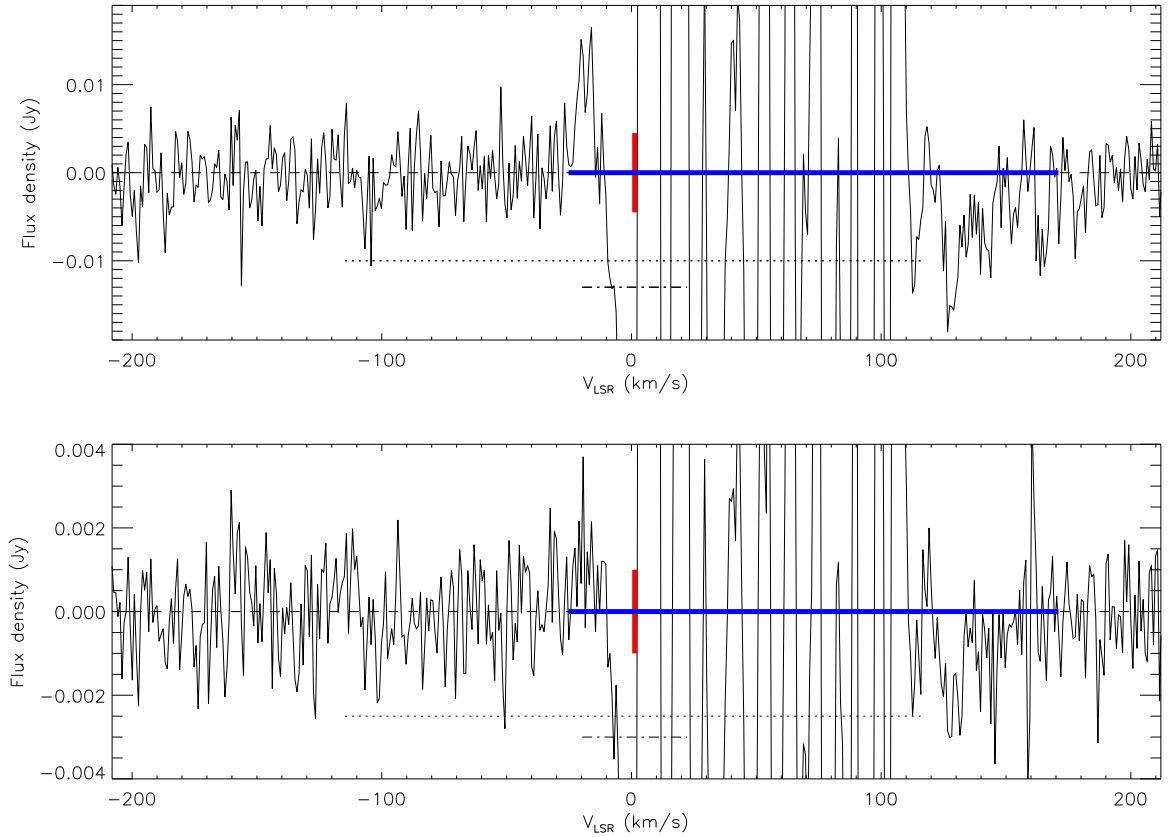

Figure 7. As in Figure 6, but for RS Pup. In the upper panel, the spectrum is integrated over a 136″ $\times$ 136″ ($\sim$1 $\times$ 1 pc) box.

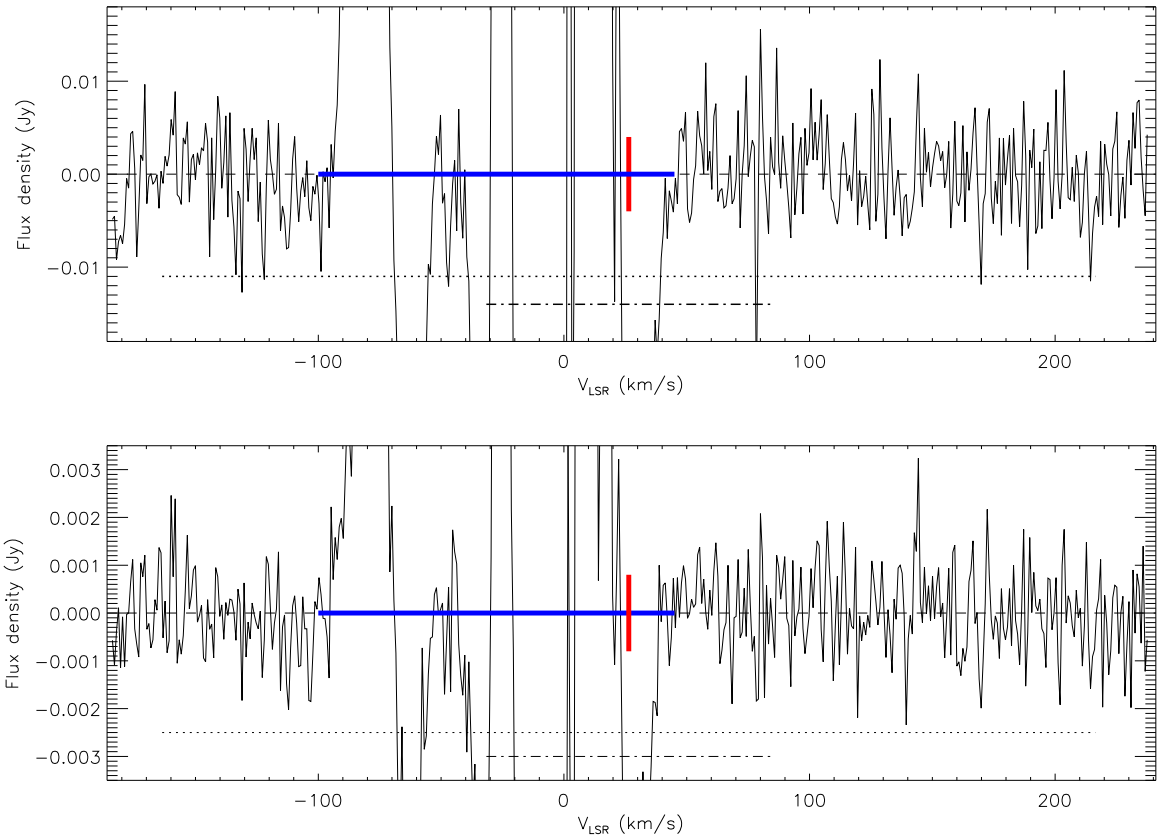

Figure 8. As in Figure 6, but for X Cyg. In the upper panel, the spectrum is integrated over a 210″ × 210″ (∼1 × 1 pc) box.

As already noted in Section 4.1 the space velocity vector of T Mon traces directly back to the approximate geometric center of the detected H I shell, consistent with the possibility that this shell could be a mass-loss remnant. However, at the same time, the fact that the star appears to be nearly completely outside the shell's boundaries implies that if it is circumstellar in origin, the shell must have formed during a *previous* epoch of mass loss that did not continue at a sustained rate to the present day. The absence of detectable emission along the leading edge of the nebula is also consistent with it being a "fossil" shell (see Wareing et al. 2007).

The interaction between the ISM and stellar ejecta affects not only the morphology of the circumstellar gas, but also its kinematics, including an appreciable deceleration of the outflowing gas at large distances from the star (e.g., Matthews et al. 2008, 2011). Qualitatively, an excess of blueshifted emission, as we see in the case of T Mon, might therefore be explained by the decelerating effect of the ISM on the ejecta (see Matthews et al. 2008). This would also imply that the red and blue peaks visible in the spectrum in Figure 5 cannot be directly interpreted as a measure of the stellar outflow speed.

Clearly numerical models that explore the interaction of mass-losing Cepheids with their environment would be of considerable interest for helping to interpret future H I observations of Cepheids. Numerical models to date have focused on AGB and post-AGB stars whose wind speeds, mass-loss rates, and mass-loss timescales all may differ significantly from Cepheids. For example, typical AGB stars have outflow velocities $V_o \sim 5$–$10\,\mathrm{km\,s^{-1}}$, which are generally several times smaller than those expected for Cepheids (see Section 6.1). This means that AGB stars are frequently in the regime where V_o is less than the space velocity V_{3D}, whereas Cepheids will more typically have $V_o \gtrsim V_{3D}$ (cf. Table 1).

5.2. Constraints on the Formation Time of a Possible T Mon Shell

As described above, the morphology of the H I nebula northwest of T Mon appears to contain a depression or cavity along its southeast edge. Possible explanations for such a cavity in a circumstellar shell could be instabilities along the leading edge of a shell (see Matthews et al. 2013) or the cessation of mass loss from the central star. Assuming the nebula lies at the same distance as T Mon, tracing the location of the star backwards along its projected space motion vector places it within this cavity at some time in the past (assuming the nebula does not have a transverse velocity component different from that of the star). Given the space velocity of T Mon (Table 1), an estimate of the travel time from the center of the apparent H I cavity to the current stellar position is $\gtrsim$38,000 yr, although this is a lower limit to the elapsed time, both because of projection effects and because it assumes that the nebula has remained stationary in the local ISM rest frame.

T Mon is believed to be currently on its third crossing of the instability strip (Turner & Berdnikov 2001), and based on Bono et al. (2000), we estimate the total lifetime of the third crossing to be $t_c \sim 26{,}000$ yr for a star of the mass and period of T Mon (assuming solar metallicity).[6] This implies that if the H I nebula comprises mass loss on the instability strip, it must have occurred during the *second* crossing, whose duration is

[6] The models of Bono et al. (2000) assume no mass loss.

Table 5
Derived Mass-loss Properties for the Target Stars

Star	V_{esc} (km s^{-1})	V_o (km s^{-1})	$\int Sdv$ (Jy km s^{-1})	M_{HI}(beam) ($M_\odot$)	$\dot{M}$(current) ($M_\odot$ yr^{-1})	M_{HI}(total) ($M_\odot$)	t_i (10^4 yr)	$\lvert\dot{M}\rvert$ ($M_\odot$ yr^{-1})
(1)	(2)	(3)	(4)	(5)	(6)	(7)	(8)	(9)
ζ Gem	183	54	<0.35	<0.012	$<1.9 \times 10^{-5}$	<0.102	4.0	$< 2.0 \times 10^{-6}$
RS Pup	116	21	<0.20	<0.112	$<1.9 \times 10^{-5}$	<0.258	140.	$<2.6 \times 10^{-7}$
X Cyg	190	58	<0.41	<0.093	$<5.6 \times 10^{-5}$	<0.288	7.2	$<5.6 \times 10^{-6}$
T Mon[a]	153	37	<0.33	<0.156	$<4.2 \times 10^{-5}$	0.4	7.0	$\sim 6 \times 10^{-6}$

Note. Explanation of columns: (1) star name; (2) escape velocity, assuming the stellar mass and radius from Table 1; (3) predicted wind outflow speed based on the relation $V_o \approx 1.6 \times 10^{-3} V_{esc}^2$ (Reimers 1977); (4) 3σ upper limit on the integrated H I flux density within a single synthesized beam centered on the star, assuming a rectangular line profile with a total linewidth of twice the estimated outflow velocity; (5) 3σ upper limit on the H I mass within a single synthesized beam centered on the star, using the integrated flux density from column 4; (6) 3σ upper limit on the current stellar mass-loss rate (see Sections 6.1 and 5 for details); (7) total detected H I mass (for T Mon) or 3σ upper limit on the H I mass within a volume of radius 0.5 pc surrounding the star; (8) estimated time spent on the instability strip based on Bono et al. (2000) (see text for details); (9) estimated mass-loss rate (or 3σ upper limit), averaged over the lifetime of the star on the instability strip.
[a] For T Mon, upper limits in columns 4–6 apply to *recent or ongoing* mass-loss, not to a period of mass loss associated with the formation of the nebula northeast of the star (see Sections 4.1 and 5).

estimated to be $t_c \sim$ 53,000 yr. (The first crossing can be largely excluded based on its short lifetime of $t_c \sim$ 3600 yr.)

5.3. Implications of Mass Loss on the Evolutionary History of T Mon

Based on Bono et al. (2001), the mass discrepancy for T Mon is $\sim$0.9 $M_\odot$, assuming models that do not include core overshoot (i.e., using "canonical masses"), while for non-canonical masses, the discrepancy would increase slightly to $\sim$0.95 $M_\odot$. These values are of the order of 10% of the mass of the star. Interestingly, this is within a factor of two of the mass we estimate for the nebula near the star ($\gtrsim 0.5 M_\odot$; Section 4.1).

Assuming this nebula indeed represents a circumstellar remnant, some fraction of its mass should have originated from material swept from the surrounding ISM. If we make a crude estimate of that contribution by assuming the distance from the Galactic Plane is $z \approx d \sin b + 15$ pc and the local ISM number density is approximately $n_H(z) = 2.0 e^{-(|z|/100\ \mathrm{pc})}$ (Loup et al. 1993), we find $n_H \approx 1.2$ cm^{-3}. Assuming a geometric mean radius for the shell of 1.0 pc (see Section 4.1), the measured atomic hydrogen mass therefore translates to a particle density $n_H \approx 3.5$ cm^{-3}, or roughly three times the expected local density. Thus it is plausible that as much as two-thirds of the shell mass ($\sim$0.4 $M_\odot$) may have had a mass-loss origin—an amount sufficient to reconcile a significant part of T Mon's mass discrepancy and to have an important impact on the evolutionary history of the star.

For a fiducial outflow speed of $\sim$40 km s^{-1} (Table 5; see also Section 6.1), a lower limit to the expansion age of the T Mon nebula is $\sim$24,000 yr. Assuming that two-thirds of the mass of the nebula was shed from the star over a comparable period would imply a mass-loss rate of $\dot{M} \lesssim 2 \times 10^{-5} M_\odot$ yr^{-1}. On the other hand, if we take as an upper limit to the age of the nebula the time that T Mon has spent on the instability strip ($\sim$70,000 yr; Bono et al. 2000), this would translate to $\dot{M} \sim 6 \times 10^{-6} M_\odot$ yr^{-1}.

The first of these two estimates is two orders of magnitude higher than the mass-loss rate estimated by Gallenne et al. (2013) based on the modeling of extended mid-IR emission [$\dot{M} \approx (5.6 \pm 0.6) \times 10^{-7} M_\odot$ yr^{-1}, after scaling to our adopted distance]. However, given that the observations of Gallenne et al. sample material within only $\sim$10–20$R_\star$, the mass-loss rate derived by those authors reflects only very recent or ongoing mass loss. As described above, H I emission is only marginally detected at the position of T Mon itself (see Figures 4 and 5, lower panel). Using the same approach as for the three undetected stars in our sample (Section 6.1), we may therefore place a 3σ upper limit on the *current* mass-loss rate for T Mon of $\dot{M} < 4.2 \times 10^{-5} M_\odot$ yr^{-1}. Our H I observations are therefore not sensitive to ongoing mass loss at a rate comparable to that estimated by Gallenne et al.

Regardless of the current mass-loss rate of T Mon, the location of the star relative to the H I nebula implies that if the nebula is circumstellar in origin, then the star must have ceased losing mass for some period of time since the nebula's formation. Combined, the new H I data and previous mid-IR results of Gallenne et al. (2013) point to a scenario where T Mon may have undergone significant variations in its mass-loss rate over the past 25,000 yr or more. This is consistent with theoretical predictions that such fluctuations will occur, particularly in long-period Cepheids (e.g., Neilson et al. 2011). Indeed, as we have noted above, this disruption could have resulted from the star temporarily leaving the instability strip after its second crossing.

Finally, it is also worth noting that T Mon, as well as δ Cep, whose circumstellar material was detected in H I by M12, are both members of triple systems. The presence of a close companion (as in the case of δ Cep) may affect the nature and intensity of mass-loss episodes. However, even companions at larger separations (present in both cases) may have an important effect on the physical properties of stellar ejecta (Mohamed & Podsiadlowski 2012; Anderson et al. 2015). While it is not possible to draw general conclusions based on a sample of only two stars, further theoretical modeling, in addition to observations of a larger sample of binary Cepheids in H I and other wavelengths sensitive to mass loss, could provide additional insights into the consequences of binarity.

6. DISCUSSION

6.1. Upper Limits on the Circumstellar H I Mass and Mass-loss Rates for the Undetected Stars

For the stars undetected in the H I line, our new VLA observations allow us to place new limits on the presence of circumstellar debris that may have been shed by these Cepheids during periods of recent or ongoing mass loss. However, translating our measurements to quantitative upper limits that

are useful for constraining the stellar mass-loss properties requires adopting some assumptions about the nature of Cepheid outflows—a topic on which we have very few empirical constraints.

To our knowledge, δ Cep is the only Cepheid with a directly measured outflow velocity ($V_o \approx 35\,\mathrm{km\,s^{-1}}$; M12). The value of V_o for δ Cep is noteworthy in that it is significantly lower than the escape speed from the star, consistent with a general trend of $V_o \ll V_{esc}$ that has been seen in other types of supergiants (Reimers 1977; Holzer & MacGregor 1985; Judge & Stencel 1991). Indeed, Reimers (1977) found that for non-variable G and K supergiants, the stars roughly follow a relation of the form $V_o \sim 1.6 \times 10^{-3} V_{esc}^2$. This relationship also holds for stars of comparable spectral type in the sample of Judge & Stencel (1991) and reasonably agrees with the measured outflow speed for δ Cep (M12), even though the underlying mass-loss mechanism may be quite different between pulsating and non-pulsating supergiants. Lacking any further constraints on V_o for Cepheids, we adopt the empirical relation of Reimers to estimate representative outflow velocities for our sample stars. These values are presented in Table 5.

If we assume that the H I linewidth for each star is approximately twice its outflow speed, we may now derive model-dependent limits on the quantity of circumstellar gas for the undetected stars. For ζ Gem and X Cyg we use the rms noise levels, σ_{rms}, from the uncontaminated portions of the naturally weighted H I data cubes in Table 4 to compute 3σ upper limits to the velocity-integrated H I flux density within a single synthesized beam centered on each of the undetected stars as $\int SdV < 3\sigma_{rms} \times (2V_o)$ Jy km s^{-1}. For RS Pup, where the entire velocity range $V_{\star,LSR} \pm V_o$ is affected by confusion (see Figure 7), we substitute for σ_{rms} the term $\sigma_{obs} = (\sigma_c^2 + \sigma_{rms}^2)^{0.5}$, where $\sigma_c = 0.66$ mJy beam^{-1} is the additional confusion noise estimated from channels with velocities between -25 and $-10\,\mathrm{km\,s^{-1}}$. For optically thin emission, the aforementioned upper limits to the integrated flux density can be translated into 3σ upper limits on the mass of H I within the synthesized beam as $M_{HI} < 2.36 \times 10^{-7} d^2 \int SdV\ M_\odot$, where d is the adopted distance in parsecs (e.g., Roberts 1975). Results are given in column 4 of Table 5.

Because the mass loss on the instability strip is expected to extend over tens of thousands of years or more, ejecta may be spread well beyond a single beam diameter—possible reaching a parsec or more from the star (see M12; Kervella et al. 2012, Section 4.1). For each undetected star, we therefore also compute upper limits on the total H I mass within a fiducial volume of radius 0.5 pc. The choice of this radius is arbitrary, but is useful for illustrative purposes. These resulting limits are given in column 7 of Table 5.

To provide an estimate of the *rate* of recent or ongoing mass-loss for each star, we assume $\dot{M} < 1.4(M_{HI}/t_c)$. Here, the factor of 1.4 accounts for the mass of helium, and the fiducial timescale t_c is taken as r_c/V_o. We adopt as the characteristic radius, r_c, the geometric mean HWHM of the synthesized beam, projected to the distance of the star. Results are given in column 5 of Table 5. We include an upper limit for T Mon, where H I was detected offset from the stellar position, but not directly along the line-of-sight to the star (see Section 5).

To constrain the *mean* mass-loss rates of ζ Gem, RS Pup, and X Cyg during their entire Cepheid evolution, we combine the volume-averaged H I mass limits computed above with estimates of the total time, t_i, that each of the stars have spent on the instability strip. We estimate t_i based on the solar metallicity models of Bono et al. (2000, their Table 7). We assume that ζ Gem is on its second crossing of the instability strip, that RS Pup and X Cyg are on their third crossings, and that the total time spent on the instability strip is equal to the sum of the previous crossings, plus one-half the predicted duration of the current crossing. The resulting time-averaged mass-loss rates, $|\dot{M}| = 1.4(M_{HI}(\mathrm{total}))/t_i$, are given in column 8 of Table 5.

6.2. Upper Limits Compared with Expected Values of $\dot{M}$

Based on recent studies of rates of period change, the mean mass-loss rate expected over the course of a Cepheid's lifetime is $\sim 10^{-7}$ to $10^{-6} M_\odot\,\mathrm{yr^{-1}}$ (Neilson et al. 2011, 2012a, 2012b). These values are comparable to the upper limits in column 8 of Table 5. The present non-detection of ζ Gem, X Cyg, and RS Pup in the H I line is therefore not in contradiction with the findings from the period change studies, and suggests that deeper H I observations may yet uncover mass-loss signatures. Furthermore, the mass-loss rate of Cepheids are not expected to be constant, but rather may vary by up to several orders of magnitude as the stars evolve along the instability strip (Neilson et al. 2011). This means that periods of intense mass loss ($\sim 10^{-5} M_\odot\,\mathrm{yr^{-1}}$) may occur, particularly for longer period Cepheids ($P >$ 15 days; Böhm-Vitense & Love 1994; Deasy 1988; Neilson & Lester 2008). While the mechanism for generating such intense mass loss is unclear, it is worth noting that because the crossing time of the instability strip is relatively short for Cepheids with periods of ~15–30 days ($<10^5$ year; Bono et al. 2000), periods of intense mass loss are likely to be required if stars in this period range (including X Cyg and T Mon) are to lose even a few percent of their mass during the Cepheid phase (see Section 6.3). For ζ Gem and RS Pup, our present upper limits on the current mass-loss rates are inconsistent with mass loss of this magnitude during the past several thousand years, but for X Cyg or T Mon it cannot be excluded (see also Section 5).

6.3. Constraints on the Role of Mass Loss for Solving the Mass Discrepancy

After scaling the upper limits to the circumstellar H I mass within a 0.5 pc radius around each star (column 7 of Table 5) by a factor of 1.4 to correct for the mass of He, it is of interest to compare the resulting masses with the stellar masses from Table 1. We find that for the three undetected stars, our limits on the mass of circumstellar matter correspond to $\lesssim$ 2%–5% of the stellar mass.

While it is difficult to accurately estimate the mass discrepancy for any individual star owing to model uncertainties, statistically, discrepancies between pulsation and evolutionary masses average between 10% and 20% (see Section 1). This tentatively suggests that for our sample stars, mass loss alone is unlikely to fully reconcile the mass discrepancy, although it could still account for a significant fraction of it. However, we stress that this conclusion is model dependent. For example, if the H I linewidths are smaller than we have assumed (e.g., as a result of deceleration of large-scale ejecta owing to interaction with the surrounding ISM), this could allow significant quantities of gas to be hidden by line-of-sight

confusion (see e.g., Le Bertre et al. 2012). Alternatively, if we have systematically underestimated the expected wind outflow velocities, the inferred upper limits would also increase.

6.4. Comparison to Past Results

A comparison between our new results and previous constraints on the mass-loss rate of T Mon were described in Section 5.3. Here we briefly compare our new results for the other three stars to earlier studies.

6.4.1. ζ Gem

For ζ Gem, Sasselov & Lester (1994) reported evidence based on the He I λ10830 line for the outflow of material in the upper chromosphere, albeit with velocities well below the escape speed (they found the mean He I line velocity to be blueshifted from the stellar velocity by 31 km s^{-1}). Ultraviolet spectroscopy by Schmidt & Parsons (1984) and Deasy (1988) also revealed possible outflow signatures in the Mg II h and k line profiles of ζ Gem (see also Deasy & Wayman 1986). In this case, two blueshifted components are seen with velocities comparable to the surface escape velocity ($\gtrsim -110$ km s^{-1} relative to the stellar systemic velocity). While it is unclear whether the large Mg II h and k velocities are reflective of the bulk outflow speed, as described in Section 4.2, we find no statistically significant emission at comparable velocities in our H I data. In any case, a wind resulting from mass loss at a rate comparable to that estimated by Deasy ($\dot{M} \sim 10^{-10}\,M_{\odot}$ yr^{-1}) would be several orders of magnitude below the detection limit of our H I observations, although it is important to stress that Deasy's $\dot{M}$ value is a lower limit, since it does not take into account the continuous flow of matter from the upper atmosphere.

6.4.2. RS Pup

The recombination line study of Gallenne et al. (2011) provided evidence of a significant quantity of atomic hydrogen in the close environment of RS Pup (i.e., on scales of ∼1″ or ∼1550 AU). Although our current spatial resolution is comparatively coarse, we are able to place a 3σ upper limit on the mass of neutral atomic hydrogen within a radius of 38,000 AU from the star (i.e., one synthesized beam) of $<0.11\,M_{\rm HI}$ (Table 5).

Looking to larger scales, Kervella et al. (2012) found a mean radius of the RS Pup reflection nebula to be 1.′8 (∼0.8 pc for our adopted distance) based on the analysis of scattered light images, and they estimated the total quantity of gas plus dust within this volume to be $190\,M_{\odot}$ (with an uncertainty of ∼40%). The assumed dust fraction is 1%. Despite the significant line-of-sight contamination in our RS Pup data, such a large quantity of gas within a region spanning only a few arcminutes in spatial extent should have been readily detectable (>5σ) in our data at velocities blueshifted by $\gtrsim -10$ km s^{-1} from the stellar systemic velocity, even if it were only ∼1% atomic. This suggests that either the nebula is predominantly molecular—consistent with the mean nucleon density of ∼2600 cm^{-3} implied from the work of Kervella et al. (2012)—or else that the atomic gas associated with the reflection nebula lies within the range of velocities where detection is hampered by line-of-sight contamination (cf. Figure 7). Last, it is worth noting that several previous authors derived much more modest mass estimates for the nebula based on dust measurements in the IR (e.g., $\sim 2.3 M_{\odot}$ (McAlary & Welch 1986); $\sim 2.2 M_{\odot}$ (Deasy 1988); ∼0.06 to $0.9 M_{\odot}$; (Barmby et al. 2011)).[7] However, in contrast to these other studies, the technique of measuring scattered light used by Kervella et al. probes additional dust content whose temperature is too low to directly emit in the IR.

Based on *IRAS* data, Deasy (1988) previously estimated the mean rate of mass loss from RS Pup to be $\sim 3 \times 10^{-6}\,M_{\odot}$ yr^{-1} (scaled to our adopted distance). However, based on the structure of the surrounding nebula, he argued that the mass loss from this star is likely to be intermittent, with episodes of enhanced mass loss at rates as high as a few times $10^{-5}\,M_{\odot}$ yr^{-1}. Our present upper limits on the mass-loss rate of RS Pup (Table 5) appear to exclude ongoing mass loss of this magnitude.

6.4.3. X Cyg

Based on *IRAS* data, McAlary & Welch (1986) noted a possible IR excess associated with X Cyg. Barmby et al. (2011) also found tentative evidence for extended IR emission around this star in their *Spitzer* images. However, in neither case are the data sufficient to estimate a mass-loss rate, and to our knowledge, no empirical limits on the mass-loss rate of X Cyg have been published to date.

7. SUMMARY

We have presented H I 21 cm line observations for a sample of four Galactic Cepheids. Our goal was to search for circumstellar gas associated with previous or ongoing mass loss. If present, such matter would help to reconcile the persistent discrepancies of ∼10%–20% between the masses of Cepheids derived from stellar evolution models versus those from the mass-dependent period–luminosity relation or orbital dynamics.

We have discovered a shell-like structure near the long-period binary Cepheid T Mon. The star lies in projection just outside the edge of this structure, with an offset from the geometric center in the direction of the star's space motion. At the distance of T Mon, the shell would have an atomic hydrogen mass of $\sim 0.4 M_{\odot}$ and a size of ∼2 pc. Although we cannot strictly exclude that the shell was formed during a red supergiant phase, or alternatively, that it represents a chance superposition of an interstellar cloud along the line-of-sight, its properties appear to be consistent with a fossil circumstellar shell that resulted from an earlier epoch of mass loss during T Mon's previous crossing of the instability strip. This interpretation would support a model where mass loss on the Cepheid instability strip is sporadic. Assuming that approximately two-thirds of the shell's mass originated from a stellar outflow, the mass of the material would be sufficient to account for ∼50% of the discrepancy between the pulsation and evolutionary mass of T Mon.

For the other three stars in our sample (RS Pup, X Cyg, and ζ Gem), no H I emission was detected that could be unambiguously associated with the circumstellar environment. In all three cases, line-of-sight confusion precluded searches of portions of the observing band, with the effect being most severe for RS Pup. For the undetected stars, we place model-dependent 3σ upper limits on the mass of circumstellar gas

[7] All of these estimates assume a gas-to-dust ratio of 100 and are scaled to our adopted distance.

within a volume of radius 0.5 pc surrounding each star. The resulting upper limits correspond to $\lesssim$2%–5% of the respective stellar masses. Given typical Cepheid mass discrepancies of ~10%–20%, mass loss through a neutral atomic wind therefore cannot yet be excluded as making a significant contribution to reconciling the discrepancy between pulsation and evolutionary mass for these stars. Furthermore, our upper limits on the mean mass-loss rates over their lifetimes on the instability strip [$\lesssim(0.3\text{–}6) \times 10^{-6}\, M_{\odot}\, \mathrm{yr}^{-1}$] are consistent with mean mass-loss rates derived from previous studies of the rate of period change of large samples of Cepheids. However, we emphasize that our current upper limits are dependent on uncertain assumptions about the properties of Cepheid winds, including the predicted outflow velocity (see Section 6.1).

The findings here, together with the previous work of M12, suggest that a deep H I survey of a larger sample of nearby Galactic Cepheids ($d \lesssim 1$ kpc) could provide additional new constraints on the role of mass loss during the Cepheid evolutionary phase. An order-of-magnitude increase in sensitivity, such as could be achieved with next-generation interferometers, would be particularly valuable. Additionally, the impact of confusion could likely be reduced in future observations through inclusion of data from longer baselines (e.g., Le Bertre et al. 2012) to help filter out the large-scale line-of-sight contamination.

L.D.M. is supported by grant AST-1310930 from the National Science Foundation. Support to N.R.E. was provided from the Chandra X-Ray Center NASA contract NAS8-03060. The observations presented here were part of NRAO program AM1087 (VLA/11B-035). This research has made use of the SIMBAD database, operated at CDS, Strasbourg, France.

REFERENCES

Anderson, R. I., Sahlmann, J., Holl, B., et al. 2015, ApJ, 804, 144
Barmby, P., Marengo, M., Evans, N. R., et al. 2011, AJ, 141, 42
Berdnikov, L. N., Henden, A. A., Turner, D. G., & Pastukhova, E. N. 2009, AstL, 35, 406
Berdnikov, L. N., Ignatova, V. V., Caldwell, J. A. R., & Koen, C. 2000, NewA, 4, 625
Böhm-Vitense, E., & Love, S. G. 1994, ApJ, 420, 401
Bono, G., Caputo, F., Cassisi, S., et al. 2000, ApJ, 543, 955
Bono, G., Caputo, F., & Castellani, V. 2006, MmSAI, 77, 207
Bono, G., Castellani, V., & Marconi, M. 2002, ApJL, 565, L83
Bono, G., Gieren, W. P., Marconi, M., Fouqué, P., & Caputo, F. 2001, ApJ, 563, 319
Bowers, P. F., & Knapp, G. R. 1987, ApJ, 315, 305
Caputo, F., Bono, G., Fiorentino, G., Marconi, M., & Musella, I. 2005, ApJ, 629, 1021
Christy, R. F. 1968, QJRAS, 9, 13
Cotton, W. D. 2008, PASP, 120, 439
Coulson, I. M. 1983, MNRAS, 203, 925
Cox, A. N. 1980, ARA&A, 18, 15
Deasy, H. P. 1988, MNRAS, 231, 673
Deasy, H. P., & Wayman, P. A. 1986, IrAJ, 17, 286
Di Benedetto, G. P. 2013, MNRAS, 430, 546
Dohm-Palmer, R. C., & Skillman, E. D. 2002, AJ, 123, 1433
Engle, S. G., Guinan, E. F., Harper, G. M., Neilson, H. R., & Evans, N. R. 2014, ApJ, 794, 80
Evans, N. R. 1984, ApJ, 281, 760
Evans, N. R. 1992, ApJ, 384, 220
Evans, N. R., Bond, H. E., Schaefer, G. H., et al. 2013, AJ, 146, 93
Evans, N. R., Carpenter, K., Robinson, R., et al. 1999, ApJ, 524, 379
Fernie, J. D., Evans, N. R., Beattie, B., & Seager, S. 1995, IBVS, 4148, 1
Flower, P. J. 1996, ApJ, 469, 355
Freedman, W. L., Madore, B. F., Gibson, B. K., et al. 2001, ApJ, 553, 47
Gallenne, A., Mérand, A., Kervella, P., & Girard, J. H. V. 2011, A&A, 527, 51
Gallenne, A., Mérand, A., Kervella, P., et al. 2013, A&A, 558, A140
Gérard, E., & Le Bertre, T. 2006, AJ, 132, 2566
Glassgold, A. E., & Huggins, P. J. 1983, MNRAS, 203, 517
Greisen, E. W. 2003, in Information Handling in Astronomy—Historical Vistas, ed. A. Heck (Dordrecht: Kluwer), 109
Havlen, R. J. 1972, A&A, 16, 252
Holzer, T. E., & MacGregor, K. B. 1985, in Mass Loss from Red Giants, ed. M. Morris & B. Zuckerman (Dordrecht: Reidel), 229
Johnson, D. R. H., & Soderblom, D. R. 1987, AJ, 93, 864
Judge, P. G., & Stencel, R. E. 1991, ApJ, 371, 357
Kalberla, P. M. W., Burton, W. B., Hartmann, D., et al. 2005, A&A, 440, 775
Keller, S. C., & Wood, P. R. 2006, ApJ, 642, 834
Kervella, P., Bersier, D., Mourand, D., Nardetto, N., & Coudédu Foresto, V. 2004, A&A, 423, 327
Kervella, P., Mérand, A., & Gallenne, A. 2009, A&A, 498, 425
Kervella, P., Mérand, A., Perrin, G., & Coudédu Foresto, V. 2006, A&A, 448, 623
Kervella, P., Mérand, A., Szabados, L., et al. 2012, A&A, 541, 18
Le Bertre, T., Matthews, L. D., Gérard, E., & Libert, Y. 2012, MNRAS, 422, 3433
Loup, C., Forveille, T., Omont, A., & Paul, J. F. 1993, A&AS, 99, 291
Marengo, M., Evans, N. R., Barmby, P., et al. 2010a, ApJ, 709, 120
Marengo, M., Evans, N. R., Barmby, P., et al. 2010b, ApJ, 725, 2392
Mariska, J. T., Doschek, G. A., & Feldman, U. 1980, ApJ, 242, 1083
Matthews, L. D., Le Bertre, T., Gérard, E., & Johnson, M. C. 2013, AJ, 145, 97
Matthews, L. D., Libert, Y., Gérard, E., Le Bertre, T., & Reid, M. J. 2008, ApJ, 684, 603
Matthews, L. D., Libert, Y., Gérard, E., et al. 2011, AJ, 141, 60
Matthews, L. D., Marengo, M., Evans, N. R., & Bono, G. 2012, ApJ, 744, 53 (M12)
Matthews, L. D., & Reid, M. J. 2007, AJ, 133, 2291
McAlary, C. W., & Welch, D. L. 1986, AJ, 91, 1209
Mérand, A., Kervella, P., Coudédu Foresto, V., et al. 2006, A&A, 453, 155
Mohamed, S., & Podsiadlowski, P. 2012, BaltA, 21, 88
Neilson, H. R., Cantiello, M., & Langer, N. 2011, A&A, 529, L9
Neilson, H. R., Engle, S. G., Guinan, E., et al. 2012a, ApJL, 745, L32
Neilson, H. R., Langer, N., Engle, S. G., Guinan, E., & Izzard, R. 2012b, ApJL, 760, L18
Neilson, H. R., & Lester, J. B. 2008, ApJ, 684, 569
Neilson, H. R., Ngeow, C.-C., Kanbur, S. K., & Lester, J. B. 2009, ApJ, 692, 81
Perley, R. 2010, EVLA Memo, 141 http://www.aoc.nrao.edu/evla/geninfo/memoseries/evlamemo141.pdf
Perley, R. A., & Butler, B. J. 2013, ApJS, 204, 19
Pietrzyński, G., Thompson, I. B., Gieren, W., et al. 2010, Natur, 468, 542
Reimers, D. 1977, A&A, 57, 395
Riess, A. G., Macri, L. M., Hoffmann, S. L., et al. 2016, ApJ, 826, 56
Roberts, M. S. 1975, in Galaxies and the Universe, ed. A. Sandage et al. (Chicago, IL: Univ. Chicago Press), 309
Sasselov, D. D., & Lester, J. B. 1994, ApJ, 423, 777
Schmidt, E. G. 2015, ApJ, 813, 29
Schmidt, E. G., & Parsons, S. B. 1984, ApJ, 279, 202
Schönrich, R., Binney, J., & Dehnen, W. 2010, MNRAS, 403, 1829
Smith, H. 1976, MNRAS, 175, 419
Turner, D. G. 1998, AJ, 116, 274
Turner, D. G. 1999, JAVSO, 27, 5
Turner, D. G., Abdel-Sabour Abdel-Latif, M., & Berdnikov, L. N. 2006, PASP, 118, 410
Turner, D. G., & Berdnikov, L. N. 2001, Odessa Astronomical Pub, 14, 170
van Leeuwen, F. 2007, A&A, 474, 653
Villaver, E., Machado, A., & Garciá-Segura, G. 2012, ApJ, 748, 94
Wareing, C. J., Zijlstra, A. A., & O'Brien, T. J. 2007, MNRAS, 382, 1233
Welch, D. L., & Duric, N. 1988, AJ, 95, 1794
Westerlund, B. 1961, PASP, 73, 72